


Disorder-order transition in multiprincipal element alloy: A free energy perspectiveXiao-Shi Wang and Yun-Jiang Wang ^{*}*State Key Laboratory of Nonlinear Mechanics, Institute of Mechanics, Chinese Academy of Sciences, Beijing 100190, China and School of Engineering Science, University of Chinese Academy of Sciences, Beijing 100049, China*

(Received 27 November 2022; revised 27 February 2023; accepted 22 March 2023; published 31 March 2023)

Although the concept of high entropy has flourished in the development of engineeringly important multiprincipal elemental crystalline materials, the role of entropy is controversial in driving possible disorder-order transition. Here we provide a thermodynamic perspective on this transition based on absolute free energy calculations of a list of equilibrated CoCrNi configurations extracted from the annealing history. A set of new physical quantities associated with the degree of anharmonicity, chemical short-range order, and Shannon-entropy-informed disorder temperatures are proposed to signify the disorder-order transition. The interrelationships between these thermodynamic quantities consistently suggest a disorder-order transition that is supported by experimental observation. The analysis further recognizes the critical role of the anharmonic effect in driving the random solid solution to a chemically short-range ordered phase. The free energy insights help us to understand the formation mechanism of locally ordered structures emerged from the solid solution of ideal mixing.

DOI: [10.1103/PhysRevMaterials.7.033606](https://doi.org/10.1103/PhysRevMaterials.7.033606)**I. INTRODUCTION**

A recent innovation in the physical metallurgy is the introduction of a category of high-entropy materials [1,2], which finds versatile applications in both mechanical and functional properties spanning a very wide range of critical service conditions [3–7]. The material design concept employs a basic rule of thermodynamics—random mixing of multiple principal elements at invariant lattice positions of crystals gives birth to high configurational entropy and, thus, lower free energy to render the thermodynamically stable solid phases of materials [8,9]. Following this philosophy, a lot of engineeringly important multiprincipal element alloys (MPEAs), or medium- to high-entropy are successfully synthesized which exhibit abnormal elastic behavior, good balance between strength and ductility due to novel plastic mechanism, unprecedented fracture toughness at cryogenic temperature, high strength at high temperature, good soft magnetic property, promising catalytic ability, as well as outstanding corrosion resistance [3–6,10–19]. Especially, the thermodynamics and mechanics of high-entropy alloys are of vast interest in material physics community in the light of both scientific curiosity and engineering significance.

The unexpected thermodynamic stability and excellent mechanical properties are attributed to the formation of possible chemical short-range order (CSRO) in the MPEAs. Both high-resolution transmission electron microscope characterizations [20–26] and atomistic simulations based on molecular dynamics and density-functional theory [27–41] provide compelling evidences toward the appearance of the short-range order in both the annealed and cast state of such alloys. The CSRO can be induced by extra thermo-mechanical processing of the as-cast MPEAs. It is a common wisdom that the

competition between enthalpic and entropic term in free energy determines the microstructure of a solid. At high temperature near the melting point of a crystalline solid, the entropic contribution is significant such that a random solid solution with ideal mixing of elements is preferred in the multicomponent alloys. However, at low temperature the enthalpic interaction between atom pairs becomes strong, sometimes enthalpy plays a dominating role such that some long- or short-range chemical order is produced in the crystalline alloys [24,42,43]. In extreme cases, one has the opportunity to notice elemental segregation or even spinodal decomposition phenomenon in multicomponent alloys. Therefore one may postulate a chemical disorder-order transition happens at appropriate thermodynamic conditions, e.g., the annealing temperature. Actually, this postulation has been confirmed in experiments [20,21].

If the spatial arrangement of atoms can be sufficiently recognized at lattice sites with advanced experimental facilities, it is easy to judge the disorder-order transition mechanism from a pure structural point of view. For example, a physically relevant phase order parameter from purely static atomic structure, and detail of its evolution path could give abundant information about the microscopic mechanism of such disorder-order transition in solid solutions [42,43]. However, this operation is an extremely challenging mission at present. Moreover, it is still controversial whether the so-called CSRO in MPEAs is a consequence of formation of real local structural pattern, or only the unavoidable interference from the crystalline planar defects in experimental characterizations [44]. In this context, how to understand the chemical disorder-order transition in MPEAs constitutes the most basic and important question in the community of materials physics and condensed matter physics.

To fully understand the physical mechanism of the disorder-order transition, the knowledge of the absolute free energy of equilibrated MPEA configurations is required along

^{*}yjwang@imech.ac.cn

the annealing path. The knowledge allows to quantitatively decouple the enthalpic and entropic contribution in free energy, which may give clear picture of the disorder-order transition mechanism from a thermodynamic point of view. However, direct calculations of free energy in MPEAs are rarely reported in the literature. This is because sampling the absolute free energy of a solid is not a trivial task [45–49]. It cannot be explicitly computed from any ensemble average of atomistic trajectories. A conventional first-order approximation of free energy is either from the harmonic, or quasiharmonic approximation, which should miss important anharmonic effect [47,50]. The latter might be an important factor that cannot be neglected in chemically complex MPEAs. Thermodynamic integration is a usual choice in sampling the absolute free energy of a system of interest, which is a standard equilibrium method [51]. However, it is time-consuming to construct a series of system Hamiltonians as the quasiequilibrium path connecting two given equilibrium states, especially in a complex system. Furthermore, it is nontrivial to implement the intermediate equilibrium states along the thermodynamic integration path. Sometimes domain knowledge is an extra requisition in this method. Remembering that the disorder-order transition involves complicated atom movements in the rugged potential energy landscape of the chemically disordered lattice [38,52], sampling the absolute free energy of MPEA along a yet not well defined cooling history seems an intricate task in atomistic simulations.

Here we provide a solution to rationalize the disorder-order transition in the MPEAs by calculation of the absolute free energy from an efficient nonequilibrium technique [45,48,49], following the Frenkel-Ladd path [53]. Comparison between the absolute free energy and the harmonic approximation reveals a critical role of anharmonicity played in the transition. Several new physical parameters including the atomic-scale Shannon entropy, chemical order parameter, and disorder temperature are also proposed to signify the transition. The interrelationships between all the discussed thermodynamic quantities give consistent criterion of the disorder-order transition. All the information provides fresh physical insights into the mechanism of the disorder-order transition in such complex concentrated alloys.

II. METHODS

A. Atomistic simulations

The force field of Co-Cr-Ni system in MD is described by an embedded-atom method (EAM) empirical potential [24], which has been extensively calibrated by both quantum mechanics calculations and experimental data in terms of lattice constant, crystalline defect energetics, elasticity and lattice vibration, plasticity, and thermodynamics of this alloy [54,55]. Each CoCrNi sample contains $N = 108\,000$ atoms with three-dimensional (3D) geometry of $\sim 106.8 \times 106.8 \times 106.8 \text{ \AA}^3$, which are large enough to guarantee the convergence of the calculated physical entities, e.g., free energy. Periodic boundary conditions and NPT ensemble (with constant number of atoms, constant stress tensor, and constant temperature) are employed in all the atomistic simulations. The temperature is controlled by the Nosé-Hoover thermostat and the stress ten-

sor is maintained zero within a Parrinello-Rahman barostat. All the atomistic simulations herein are performed using the LAMMPS code [56]. The OVITO package is used to visualize the atomic configurations of MPEAs [57].

We prepare a list of the equilibrium configurations for the CoCrNi MPEAs by a hybrid simulation protocol involving both molecular dynamics (MD) and Monte Carlo (MC) simulations at various annealing temperatures ranging from 300 to 1600 K. In the simulation combination of MD and MC, each accepted MC swap is followed by MD simulation [24,54,58]. In each one MC cycle, a significant fraction of $N/4$ atoms swap randomly within every 20 MD steps. The MD time step is 2.5 femtosecond. The considered high temperature is approaching the melting point (1675 K) of this alloy. The MC is used to find the lower and final stable thermodynamic states, and MD conducted after each MC is used to record the potential energy of the system. A key parameter to guarantee the equiatomic concentration of compositions in the multicomponent alloy is the chemical potential differences between elemental pairs, which are adopted $\Delta\mu_{\text{Ni-Co}} = 0.021 \text{ eV}$, $\Delta\mu_{\text{Ni-Cr}} = -0.031 \text{ eV}$ that have been validated as suitable choices [24]. Sufficient MC cycles up to 1 000 000 are applied in the cases of 300–800 K, and 50 000 cycles for the samples at temperature 900–1600 K to reach the respective equilibrium configurations of CoCrNi.

B. MSD and spring constant

The vibrational mean-squared displacement (vMSD) of atoms, or MSD, is defined as

$$\langle \Delta r_i^2 \rangle = \langle |\mathbf{r}_i(t) - \mathbf{r}_{i,\text{equil}}|^2 \rangle_\tau. \quad (1)$$

Here $\mathbf{r}_i(t)$ is the instantaneous position of the atom i at time t during thermodynamic equilibration for 100 ps. Such a suitable time duration makes sure that the atoms vibrate around their thermodynamic equilibrium positions without escaping from the original lattice in the solid state. $\mathbf{r}_{i,\text{equil}}$ is the time-invariant equilibrium position of this atom at the lattice site after energy minimization, which is equivalent to the time average of $\mathbf{r}_i(t)$. The angular brackets imply time average during the observation time τ . After this operation, the atomic-scale spring constant of the Einstein crystal is determined by

$$k = 3k_B T / \langle \Delta r_i^2 \rangle, \quad (2)$$

with k_B the Boltzmann constant and T the absolute temperature in Kelvin. Another parameter $\langle \Delta r_i^2 \rangle^{1/2} / a_0(T)$ is calculated based on the MSD at temperature T , where $a_0(T)$ is the lattice constant of the configuration at temperature T . It is the relatively vibrational amplitude that can effectively inform the characteristics of solids near the melting point.

C. Absolute free energy

We adopt a nonequilibrium thermodynamic integration method to calculate the absolute free energy of the MPEAs following the Frenkel-Ladd path, as implemented by Freitas *et al.* in LAMMPS [48]. The Frenkel-Ladd method computes the free energy difference between two specific equilibrium states by connecting by a list of nonequilibrium intermediate states [53]. The method has been validated in calculations of free

energies of bulk crystal [48], crystalline defect [49], as well as liquid and glass [45,59]. Generally, it allows the calculation of any free energy difference of a given Hamiltonian $H(\lambda)$ by interpolation between two ends

$$H(\lambda) = \lambda H_f + (1 - \lambda)H_i, \quad (3)$$

where H_i and H_f represent the Hamiltonians of the initial and final state, respectively. λ is a order parameter which characterizes the thermodynamic state of a system between the initial and final one.

Following the definition, the free energy difference between the final and initial state $\Delta F = F_f - F_i = \int_0^1 d\lambda (H_f - H_i)_\lambda$ by the Hamiltonian interpolation. In the nonequilibrium estimation of free energy difference in an intermediate state at time t_s by MD sampling, the forward work done is

$$W_{i \rightarrow f}^{\text{irr}} = \int_0^{t_s} dt \frac{d\lambda}{dt} [H_f(\Gamma(t)) - H_i(\Gamma(t))]. \quad (4)$$

Here $\Gamma(t)$ is the phase space trajectory of the system along the process. The backward work is in a similar form of $W_{f \rightarrow i}^{\text{irr}} = \int_0^{t_s} dt \frac{d\lambda}{dt} [H_i(\Gamma(t)) - H_f(\Gamma(t))]$.

In this work, the initial Hamiltonian H_i is chosen to be the system of interest, the free energy of which is calculated with respect to a reference system with fixed Hamiltonian H_f and known free energy. The classical Hamiltonian of the system of interest is

$$H_i = \sum_i^N \frac{\mathbf{p}_i^2}{2m} + U(\mathbf{r}), \quad (5)$$

where \mathbf{p}_i is momentum of the i th particle, m is the particle mass, and $U(\mathbf{r})$ is the potential energy, respectively. For a system of noninteracting particles of mass m , each atom is attached to a lattice point by a 3D harmonic spring with elastic constant k . The crystallographic lattice to which these particles are connected corresponds precisely to that of the equilibrium phase of system with H_f , which is actually an Einstein crystal with $3N$ independent vibrations. Consequently, the Hamiltonian of this harmonic system is rewritten as

$$H_f \equiv H_{\text{Einstein}} = \sum_{i=1}^N \left[\frac{\mathbf{p}_i^2}{2m} + \frac{1}{2} m \omega^2 (\mathbf{r}_i - \mathbf{r}_{i,\text{equil}})^2 \right], \quad (6)$$

where ω is the vibrational frequency and N is the number of atoms in the system. The free energy of Einstein crystal is known analytically as

$$F_{\text{Einstein}}(N, V, T) = 3N k_B T \ln \left(\frac{\hbar \omega}{k_B T} \right), \quad (7)$$

with \hbar the Planck's constant.

Note that the work associated with the initial and final states involves both the forward and backward switching processes. Taking average of the two processes will eliminate the energy dissipation during the nonequilibrium thermodynamic integration. Standard equilibrium method to calculate the free energy difference ΔF , which is based on the two equilibrium states determined by calculating the relevant thermodynamic mean values of these states through a set of independent equilibrium simulations. The reversible work

W_{rev} is done along the quasistatic path connecting them. However, the nonequilibrium approach assumes this path as a clearly time-dependent process, where the time duration of this process determines the deviation from the quasistatic path. Therefore the free energy difference $\Delta F = W_{\text{rev}} = \overline{W_{\text{irr}}} - \overline{E_{\text{diss}}}$, where the $\overline{W_{\text{irr}}}$ is the mean work and $\overline{E_{\text{diss}}}$ is the mean dissipated heat produced by a series of the nonequilibrium processes. If the nonequilibrium process is sufficiently close to the ideal quasistatic process, the dissipated heat which is systematic error becomes the same for the two processes, which proceed in opposite directions. For example, for a linear response, nonequilibrium process connecting states 1 and 2, the dissipated heat $E_{\text{diss}}^{1 \rightarrow 2} = E_{\text{diss}}^{2 \rightarrow 1}$, so that the free energy difference $\Delta F = F_2 - F_1 = \frac{1}{2} (W_{1 \rightarrow 2}^{\text{rev}} - W_{2 \rightarrow 1}^{\text{rev}}) = \frac{1}{2} (W_{1 \rightarrow 2}^{\text{irr}} - W_{2 \rightarrow 1}^{\text{irr}})$. The systematic error can be eliminated by combining the calculation of the forward and backward processes. Therefore the time-dependent nonequilibrium process can be estimated from several relatively short simulations, and its convergence can be systematically verified. In sum, the free energy of interest F_i can be estimated as

$$F_i(N, V, T) = F_{\text{Einstein}}(N, V, T) + \frac{1}{2} (\overline{W_{i \rightarrow f}^{\text{irr}}} - \overline{W_{f \rightarrow i}^{\text{irr}}}). \quad (8)$$

In this work, we have chosen a reasonable equilibration time of 10 000 MD steps before starting the nonequilibrium switching process. The forward and backward switching takes 85 000 MD steps, respectively. The spring constant k of the reference Einstein crystal, and thus the vibrational frequency ω , is obtained by measuring the MSD as described in the method section.

D. Shannon entropy and chemical short-range order parameter

To measure the global degree of CSRO in a multi-component alloy, we first propose a quantitative metric of atomic-scale Shannon information entropy

$$S_{i,\text{Shannon}} = -k_B \sum_{\alpha}^n x_{\alpha} \ln x_{\alpha}, \quad (9)$$

here x_{α} is the probability of finding one type of the atom around the central atom, and $n = 3$ the number of compositions in the studied alloy. The atoms are selected by all the nearest neighbors of the central atom based on the FCC lattice, where the spatial radius from the central atom to the nearest atom is determined by the position of the first peak of the radial distribution function. In the case of intermetallics, there is long-range chemical order and the sequence of atoms around a central atom is well defined. Therefore the Shannon entropy is zero. In the case of a random solid solution, the probability of finding a neighboring element is $1/n$ such that the entropy is maximized with $S_{i,\text{Shannon}} = 1.09$. To further quantify the degree of chemical order of a multicomponent system, a global parameter is defined after the Shannon entropy via

$$\varphi = \langle \exp(-S_{i,\text{Shannon}}/k_B) \rangle_N, \quad (10)$$

here $\langle \dots \rangle$ denotes the average over all the atoms and chemical species in the alloy system. φ is always between 0 and 1 in mathematics. In the present ternary CoCrNi system, $\varphi =$

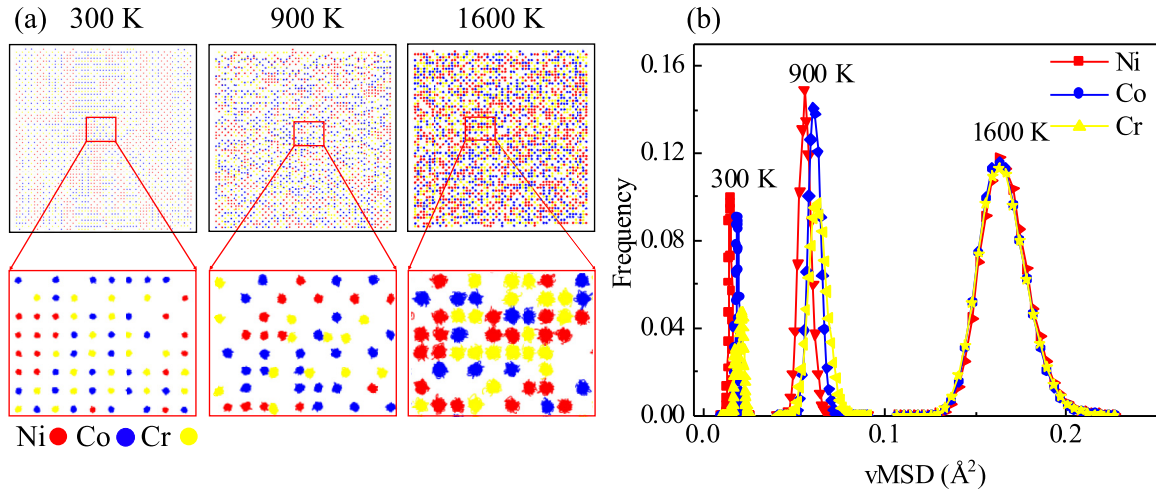


FIG. 1. Atomic vibration and spring constant in CoCrNi MPEA. (a) Spatial illustration of the trajectories of distinct atoms at 300, 900, and 1600 K, respectively. The red boxes in the lower panels are magnified from the selected area in the upper panels. (b) The distribution of the MSD for different type of atoms at 300, 900, and 1600 K, respectively.

0.336 represents the totally disordered random solid solution, and $\varphi = 1$ denotes an ordered intermetallic, respectively.

III. RESULTS

Before going to the free energy calculations, we first test the vibrational nature of the atoms in this CoCrNi MPEAs. For this purpose, the MSD is demonstrated as a spatial nature in Fig. 1(a). This plot shows the trajectories of atoms during an equilibration time of 100 ps to estimate the MSD. From the amplified slices taken from one atom layer shown in the lower panels, one can notice diversity in the vibrational amplitudes of different atoms.

For a quantitative comparison, the histograms of MSD for different elements are summarized in Fig. 1(b) at different temperatures. While it is straightforward that higher temperature gives larger vibrational amplitude and wider distribution in MSD, the vibration in MPEAs brings about new temperature-dependent phenomena. At low temperature, the MSD of Co, Cr, and Ni are well distinguished. Among them, MSD of Ni is the smallest, and Cr presents the largest MSD. It means that the Ni atoms are most strongly constrained rather than the other two type of atoms. However, this trend is broken at high temperature, e.g., the case of 1600 K. At such high temperature, the MPEA becomes almost random solid solution such that all the three type of atoms demonstrate the same distribution of MSD. The observation implies that local atomic environment becomes homogeneous and all the atoms become feel the same constraint. Therefore they are indistinguishable in vibration in the case of ideal mixing. However, some chemical segregation or even CSRO form at low temperature. Then, the local atomic stiffness is different and MSD diverge for different elements.

Once the MSDs are available, one has the opportunity to examine the atomic-scale stiffness in this list of MPEAs in light of the spring constants [60]. In Fig. 2(a), the spring constants of different elements are displayed as a function of temperature. There are several conclusions can be drawn from this plot. First, the spring constants, or vibration con-

straints, of these elements are different. Among them, Ni feels the strongest constraint and thus has the largest spring constant. This observation is in agreement with the smallest

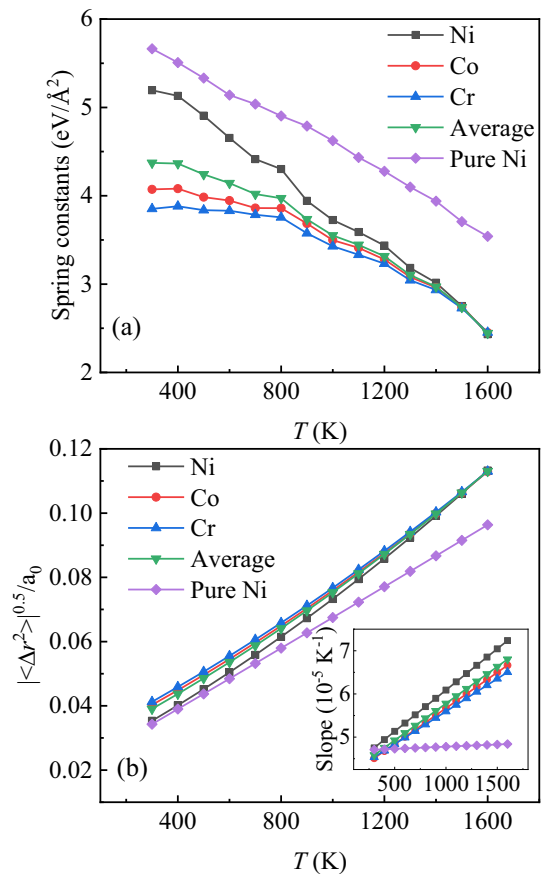


FIG. 2. Lattice constraints of the elements in CoCrNi MPEAs, in comparison with that in the elemental Ni. (a) Evolution of the spring constant as a function of temperature. (b) The ratio of MSD to lattice constant (i.e., Lindemann parameter) versus temperature. (Inset) The slope of the curves in the main plot.

MSD noticed from Fig. 1(a). Next, the diversity in atomic stiffness becomes smaller at higher temperature. At high temperature 1600 K near melting, all the spring constants converge to a single value, indicating that the elastic field becomes more homogeneous in this alloy if random solid solution is approximated. Then, the spring constant decreases with increasing temperature, which is a natural consequence of the thermal softening effect due to phonon. However, the gradient of decrease in these curves varies remarkably with temperature. This is a signal that is in striking contrast with that of an elemental FCC Ni, as illustrated by the purple line in Fig. 2(a). It might also mean that the atomic environment of CoCrNi varies while the lattice is always FCC according to temperature. The short-range ordering is driven by the competition between enthalpic and entropic interactions. The spring constant of a pure FCC Ni is shown in purple rhombus line, which decreases linearly with increasing temperature. Obviously, the MPEA is of more anharmonic nature than a single elemental metal. Finally, the temperature-dependent spring constants of the compositions are indicative of different free energy trend at different temperature. Free energy might tell something about the driving force for the disorder-order transition upon cooling in MPEAs from a physical perspective.

It is then worth testing the validity of Lindemann melting criterion in MPEAs since all the MSDs and lattice constants are available at different temperatures up to melting. The well-known Lindemann melting criterion claims that the melting of a crystalline solid happens once the MSD from the equilibrium position reaches a critical value of about 0.1 of the lattice constant [61]. Although the criterion has been widely assumed in the conventional solids with a threshold between 0.1 and 0.2 [62–66], the validity of this empirical rule is largely unknown since the complex atomic environment already generates strong lattice distortion instead of the thermal MSD far below the lattice instability point. In Fig. 2(b), the ratio of MSD to lattice constant $\langle \Delta r_i^2 \rangle^{1/2} / a_0(T)$ (i.e., the Lindemann parameter) is shown as a function of temperature. Note that here we test the Lindemann proposition in the bulk form as a first approximation, which neglects the pre-melting mechanism from crystalline defects such as surface. In comparison, we also show the data for pure Ni. It is clear that the ratio increases with temperature in both MPEA CoCrNi and pure Ni, as predicted by the Lindemann criterion. However, pure Ni shows a linear relationship in the temperature-dependent Lindemann parameter whereas the trend in MPEA is strongly nonlinear, as illustrated by the slopes shown in the inset of Fig. 2(b). The melting point of this CoCrNi alloy is 1675 K based on this EAM potential [24]. Upon approaching the melting point, the Lindemann parameters of the three constitute atoms converge to a single value of about 0.12. This critical magnitude of MSD lies well in the prediction of the Lindemann melting criterion. However, the chemical discontinuity in MPEA could lead to partial local disordering which renders different atomic mechanism of melting in bulk multicomponent alloys that is in contrast with the picture obtained from pure elemental metals [67].

With the knowledge about the MSD and the atomic-scale elastic constants, we are able to calculate the absolute free energy of the CoCrNi MPEA as a function of temperature, which

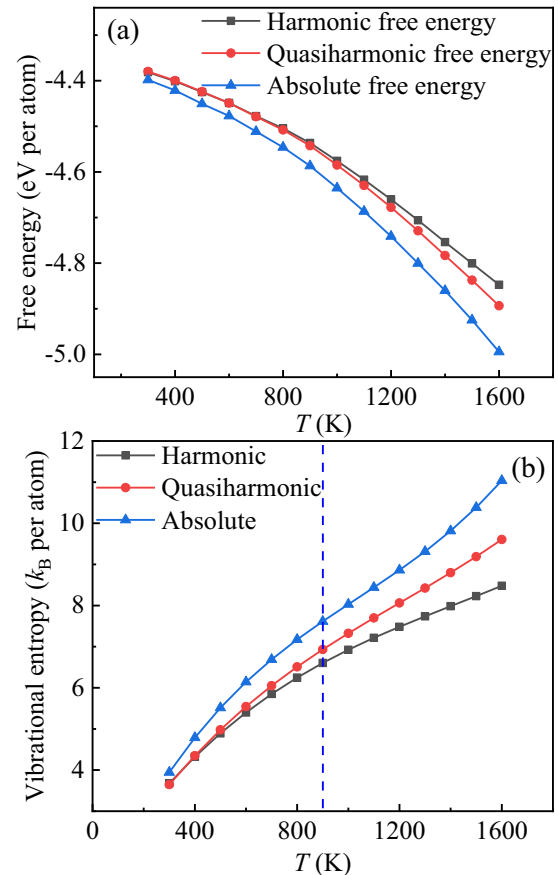


FIG. 3. Free energy and entropy. (a) Free energies of the CoCrNi MPEA as a function of temperature, which include the absolute free energy from Frenkel-Ladd method, and these calculated from harmonic and quasiharmonic approximations, respectively. (b) The corresponding vibrational entropies calculated by taking derivatives of the free energies with respect to temperature.

are summarized in Fig. 3(a). To get deeper insight into the anharmonic effect in this alloy, we also show the free energy determined from either harmonic or quasiharmonic approximation, which are provided together in Fig. 3(a). In contrast with the Einstein model, the vibrational density of states $g(\omega)$ of a real solid are calculated by taking the Fourier transform of the velocity auto correlation function during a canonical MD sampling of vibration, i.e., $g(\omega) = \int_0^\infty e^{i\omega t} \frac{\langle \mathbf{v}(t) \cdot \mathbf{v}(0) \rangle}{\langle \mathbf{v}(0) \cdot \mathbf{v}(0) \rangle} dt$. In the framework of harmonic approximation, $g(\omega)$ is estimated at extremely low temperature. The quasiharmonic approximation framework further considers the thermal expansion effect and $g(\omega)$ is recalculated with varied simulation box whose size changes with temperature. Then the vibrational free energy of the system is determined from vibrational density of states via

$$F_{\text{vib}}(T) = k_B T \int_0^\infty g(\omega) \ln \left[1 - \exp \left(-\frac{\hbar \omega}{k_B T} \right) \right] d\omega \quad (11)$$

since phonon obeys the Bose statistics. From the difference in free energies as shown in Fig. 3(a), which are obtained by different theoretical protocols, one can find strong anharmonic effect in this CoCrNi alloy. Either harmonic or quasiharmonic

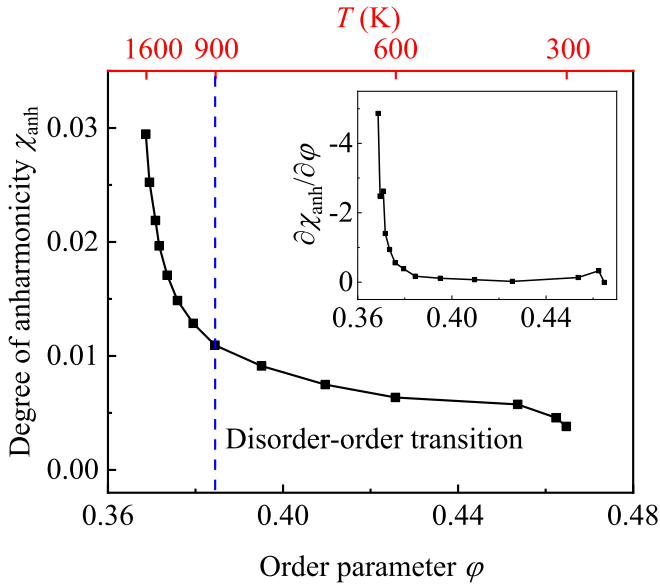


FIG. 4. Evolution of the degree of anharmonicity χ_{anh} as a function of the chemical order parameter, which indicates a disorder-order transition at 900 K in this CoCrNi MPEA. (Inset) The slope of the curves in the main plot.

approximation overestimates the absolute free energy. The anharmonicity becomes more remarkable at higher temperature.

Since free energy is the king parameter measuring the thermodynamic stability of a solid matter, one may expect to see some discontinuity in its nature of temperature dependence. However, such anomaly is not directly noticed in Fig. 3(a). To seek for a physical signature for the existence of some chemical disorder-order transition in this alloy, we further calculate the temperature-dependent vibrational entropy in Fig. 3(b) by taking differential of the free energy curve with respect to temperature, i.e.,

$$S_{\text{vib}}(T) = -\frac{\partial F_{\text{vib}}(T)}{\partial T}. \quad (12)$$

Obviously, the absolute vibrational entropy is larger than the those from either harmonic or quasiharmonic approximation in the whole temperature range of interest. It is quite interesting to see an inflection point at 900 K in the absolute vibrational entropy. This inflection point possibly indicates a disorder-order transition in the CoCrNi alloy. Careful examination of the variation gradient in entropy from harmonic or quasiharmonic approximation also tells something useful. The slopes both exhibit crossover point at 900 K. All the information suggests possible structural transition happening at 900 K in this MPEA.

In order to quantitatively analyze the anharmonic contribution to the absolute free energy, we define a parameter to characterize the degree of anharmonicity via

$$\chi_{\text{anh}}(T) = \frac{F_{\text{abs}}(T) - F_{\text{har}}(T)}{F_{\text{abs}}(T)}, \quad (13)$$

in which the absolute free energy $F_{\text{abs}}(T)$ [from Eq. (8)] and the harmonic free energy $F_{\text{har}}(T)$ [from Eq. (11)] have been shown in Fig. 3(a). This parameter is shown in Fig. 4 versus both the CSRO parameter ϕ and temperature. It is intriguing

to discover that the chemical order is a strong function of the degree of anharmonicity χ_{anh} . At 900 K, the disorder-order transition occurs as informed simultaneously by the degree of anharmonicity and CSRO. The inset of Fig. 4 is the gradient of the main plot, which clearly demonstrates the critical point at $\phi = 0.385$. It is corresponding to the MPEA configuration prepared at 900 K by the hybrid MD/MC annealing. Since the anharmonicity parameter χ_{anh} is directly from the free energy data, we therefore predict the chemical disorder-order transition in this CoCrNi MPEA from a free energy point of view.

IV. DISCUSSION

The chemical disorder-order transition is not like that of the structural phase transition, e.g., the liquid-solid transition. In the latter case, positional rearrangement of atoms can be observed intuitively by any suitable experimental characterization or atomistic simulation method. However, the chemical disorder-order transition only involves exchange of elements at specific lattice sites that is invariant, which is hard to distinguish. To comprehend this chemical disorder-order transition in MPEA upon cooling from high temperature in the solid solution, herein we discuss the relationship between a set of important physical entities, either from calculation or rationale proposition based on simulation data. This strategy avoids the difficulty of analyzing transition from a pure structural perspective. It therefore provides an alternative view solution to understand the disorder-order transition in MPEAs. The discussed entities include the absolute free energy, the chemical order parameter, potential energy, Shannon entropy and its conjugate disorder temperature, as well as the thermodynamic temperature. All the interrelationships between them are shown and explained in Fig. 5.

First of all, the relationship between the absolute free energy [from Eq. (8)] and the chemical order parameter is shown in Fig. 5(a). The absolute free energy decreases as the order parameter decreases, along with increase in temperature. It is a natural consequence that the free energy is lower for the samples annealed at lower temperature. It means that the change in both enthalpic interaction as well as entropy plays a critical role in driving the evolution of configuration upon cooling. There is a sharp downward trend starting from 900 K, which indicates a dramatic disorder-order transition at $\phi = 0.385$. This observation is in good agreement with the scenario in the degree of anharmonicity, as shown in Fig. 4. The argument is also supported by experiment [21]. When the CoCrNi sample is annealed sufficiently at 1000 °C, the short-range order forms and produces higher stacking fault energy and hardness in this concentrated alloy.

Next, in Fig. 5(b), we report the correlation between the potential energy per atom and the average value of the atomic-scale Shannon entropy ($s_{\text{Shannon}} = \langle s_{i,\text{Shannon}} \rangle$). The latter quantity characterizes the information entropy of diversity of elements occupying the FCC lattice sites and therefore, the chemical disorder of the distribution of elements in the CoCrNi MPEA. It is clear that the potential energy is positively correlated with Shannon entropy—more chemically disordered configuration with higher potential energy. The relationship shows a trend of exponential growth in potential

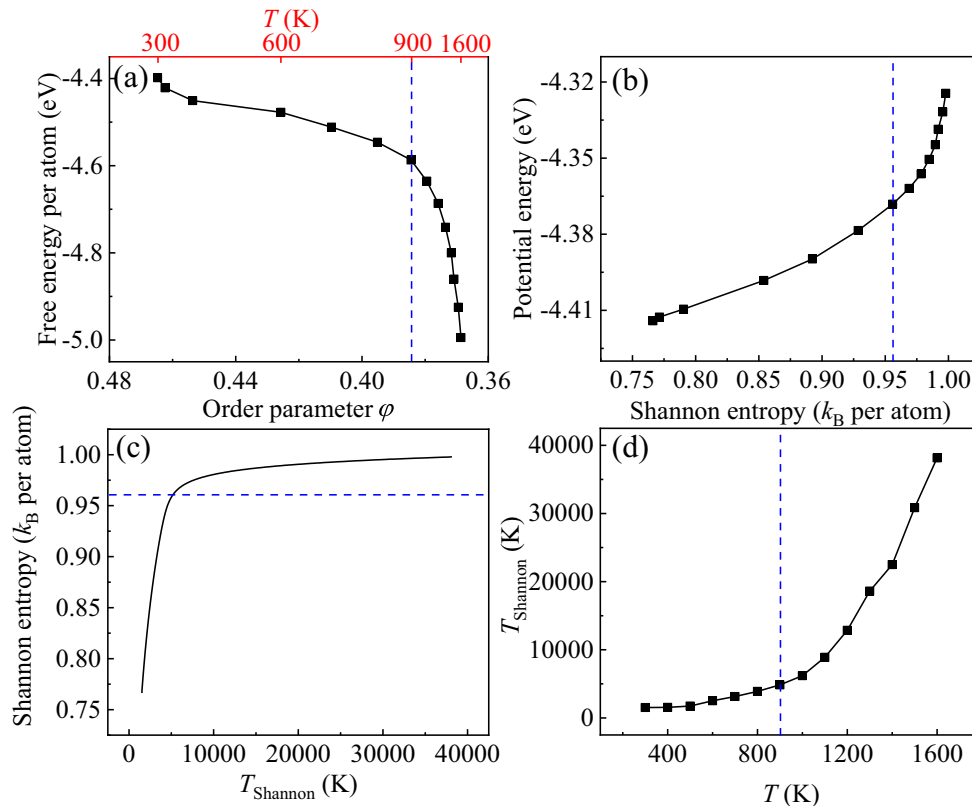


FIG. 5. The chemical disorder-order transition in CoCrNi MPEA signified by the interrelationships between different thermodynamic quantities. (a) Absolute free energy versus chemical order. (b) Potential energy versus Shannon entropy. (c) Shannon entropy versus the disorder temperature. (d) Disorder temperature versus thermodynamic temperature. In all the figures, the vertical or horizontal dash lines in blue indicate the critical point of the disorder-order transition.

energy with a strong upturn at Shannon entropy $0.96k_B$. This value is just corresponding to temperature 900 K at which the disorder-order transition takes place.

Then, from the relationship between potential energy and Shannon entropy in Fig. 5(b), it is physically meaningful to define an effectively disorder temperature T_{Shannon} through

$$T_{\text{Shannon}} = -\frac{\partial E_{\text{pot}}(T)}{\partial s_{\text{Shannon}}}, \quad (14)$$

in which $E_{\text{pot}}(T)$ is the potential energy per atom for the equilibrium configuration of MPEA annealed at T . Note that the defined disorder temperature is only a measure of degree of chemical disorder that is quantitatively different from the thermodynamic temperature T . Figure 5(c) illustrates how the Shannon entropy is modulated by the disorder temperature. As the disorder temperature increases the Shannon entropy rises significantly until to a critical point with $s_{\text{Shannon}} = 0.96k_B$, after which the growth rate is drastically slowed down. This critical point is again corresponding to the disorder-order transition. In this way, the disorder temperature is validated to be a suitable metric to signify the disorder-order transition in MPEA. Such a definition of the disorder temperature can be generally used to study the nonequilibrium process of any meta-stable multicomponent alloy from atomistic simulations.

Last but not the least, the two kinds of temperatures—the chemical disorder temperature and the thermodynamic temperature—are compared in Fig. 5(d). Basically, there a

positive scaling between disorder temperature and thermodynamic temperature. Besides, an interesting observation is that the curve presents two regimes with 900 K as a critical point separating the high-temperature and low-temperature regimes. Consequently, the $T_{\text{Shannon}}-T$ relationship is also able to indicate the disorder-order transition in CoCrNi alloy. In the high-temperature regime, the chemical disorder loses quickly following a typical equilibrium cooling path. The chemical order are mostly established in this regime. When the state goes into the low-temperature regime, the chemical order is almost frozen although disorder temperature still evolves mildly with the change in temperature. Such information is meaningful to the experimentalists working at optimization of the mechanical properties of MPEAs by controlling the microstructure via proper heat treatment process during materials fabrication.

V. CONCLUSION

The driving force and the physical mechanism of chemical ordering constitute a central unsolved problem in the generic high-entropy alloys. The missing quantity is the absolute free energy during a whole annealing process. In this context, this work provides a comprehensive free energy perspective on the obscure chemical disorder-order transition in a prototypical CoCrNi MPEA via atomistic simulations. For this purpose, we extensively calculate the free energy of the equilibrium MPEA samples prepared at different temperatures via

a hybrid MD/MC simulation protocol. The free energies are from the nonequilibrium thermodynamic integration through a Frenkel-Ladd path, the harmonic approximation, as well as the quasiharmonic approximation, respectively. It allows to quantitatively assess the role of anharmonicity played in the disorder-order transition in this multicomponent alloy. We also propose a set of new parameters, including the degree of chemical order φ , the atomic-scale Shannon entropy s_{Shannon} , the chemical disorder temperature T_{Shannon} , respectively. The interrelationships among all these quantities together with temperature and free energy are fully discussed. All the correlations are found effective in indicating a crossover point in the cooling history, consistently providing a complete picture of the chemical disorder-order transition in this CoCrNi alloy. The proposed methodology is general to study the structural evolution of any multicomponent alloy from a thermodynamic point of view via performing atomistic simulations and free energy samplings.

ACKNOWLEDGMENTS

This work was financially supported by the National Natural Science Foundation of China (Grant No. 12072344) and the Youth Innovation Promotion Association of the Chinese Academy of Sciences. The numerical calculations in this study were carried out on the ORISE Supercomputer.

APPENDIX: SHANNON ORDER PARAMETER VERSUS WARREN-COWLEY PARAMETER

In our work, the Shannon entropy is a statistical metric of the distribution of different kinds of atoms around the central atom. Similarly, the chemical order parameter φ represents the distribution of local atoms, which is derived after the Shannon

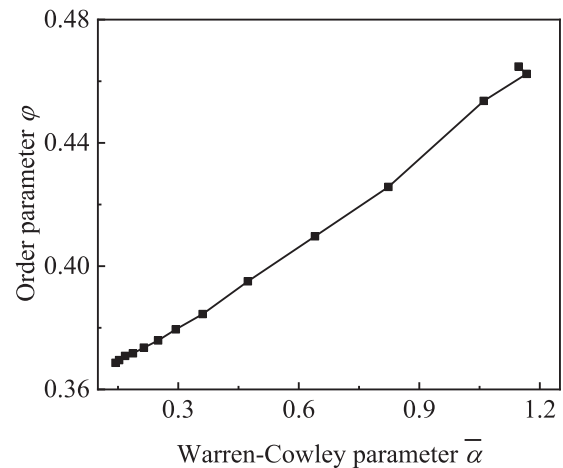


FIG. 6. Order parameter φ as a function of the mean Warren-Cowley parameter $\bar{\alpha}$ over all possible pairs.

entropy. In order to show the effectiveness of our new metric, we further calculate the Warren-Cowley parameters $\alpha_{ij} = 1 - \frac{p_{ij}}{c_j}$ of atom pairs, where p_{ij} is the probability of finding a j -type atom around an i -type atom in the nearest neighbor shell, and c_j is the nominal concentration of the j -type atom in the chemically disordered system. The mean Warren-Cowley parameter $\bar{\alpha} = \frac{|\sum_i^M \alpha_{ij}|}{M}$, where M is the number of pair types. The relationship between the order parameter φ and the mean pair SRO parameter $\bar{\alpha}$ is further shown in Fig. 6. It can be clearly seen that there is a positive correlation between them. Therefore the order parameter φ based on Shannon entropy can also represent the local atomic distribution. The advantage of the Shannon entropy order parameter is that it can reflect the level of chemical order at the system level with a single parameter.

-
- [1] J.-W. Yeh, S.-K. Chen, S.-J. Lin, J.-Y. Gan, T.-S. Chin, T.-T. Shun, C.-H. Tsau, and S.-Y. Chang, Nanostructured High-Entropy Alloys with Multiple Principal Elements: Novel Alloy Design Concepts and Outcomes, *Adv. Eng. Mater.* **6**, 299 (2004).
 - [2] B. Cantor, I. Chang, P. Knight, and A. Vincent, Microstructural development in equiatomic multicomponent alloys, *Mater. Sci. Eng. A* **375-377**, 213 (2004).
 - [3] B. Gludovatz, A. Hohenwarter, D. Catoor, E. H. Chang, E. P. George, and R. O. Ritchie, A fracture-resistant high-entropy alloy for cryogenic applications, *Science* **345**, 1153 (2014).
 - [4] Z. Li, K. G. Pradeep, Y. Deng, D. Raabe, and C. C. Tasan, Metastable high-entropy dual-phase alloys overcome the strength-ductility trade-off, *Nature (London)* **534**, 227 (2016).
 - [5] Q. Ding, Y. Zhang, X. Chen, X. Fu, D. Chen, S. Chen, L. Gu, F. Wei, H. Bei, Y. Gao, M. Wen, J. Li, Z. Zhang, T. Zhu, R. O. Ritchie, and Q. Yu, Tuning element distribution, structure and properties by composition in high-entropy alloys, *Nature (London)* **574**, 223 (2019).
 - [6] P. Shi, R. Li, Y. Li, Y. Wen, Y. Zhong, W. Ren, Z. Shen, T. Zheng, J. Peng, X. Liang, P. Hu, N. Min, Y. Zhang, Y. Ren, P. K. Liaw, D. Raabe, and Y. D. Wang, Hierarchical crack buffering triples ductility in eutectic herringbone high-entropy alloys, *Science* **373**, 912 (2021).
 - [7] E. P. George and R. O. Ritchie, High-entropy materials, *MRS Bull.* **47**, 145 (2022).
 - [8] Y. F. Ye, Q. Wang, J. Lu, C. T. Liu, and Y. Yang, High-entropy alloy: Challenges and prospects, *Mater. Today* **19**, 349 (2016).
 - [9] E. P. George, D. Raabe, and R. O. Ritchie, High-entropy alloys, *Nat. Rev. Mater.* **4**, 515 (2019).
 - [10] L. Han, F. Maccari, I. R. Souza Filho, N. J. Peter, Y. Wei, B. Gault, O. Gutfleisch, Z. Li, and D. Raabe, A mechanically strong and ductile soft magnet with extremely low coercivity, *Nature (London)* **608**, 310 (2022).
 - [11] J. Ren, Y. Zhang, D. Zhao, Y. Chen, S. Guan, Y. Liu, L. Liu, S. Peng, F. Kong, J. D. Poplawsky, G. Gao, T. Voisin, K. An, Y. M. Wang, K. Y. Xie, T. Zhu, and W. Chen, Strong yet ductile nanolamellar high-entropy alloys by additive manufacturing, *Nature (London)* **608**, 62 (2022).
 - [12] H. Li, H. Zong, S. Li, S. Jin, Y. Chen, M. J. Cabral, B. Chen, Q. Huang, Y. Chen, Y. Ren, K. Yu, S. Han, X. Ding, G. Sha, J. Lian, X. Liao, E. Ma, and J. Sun, Uniting tensile ductility with ultrahigh strength via composition undulation, *Nature (London)* **604**, 273 (2022).

- [13] Q. F. He, J. G. Wang, H. A. Chen, Z. Y. Ding, Z. Q. Zhou, L. H. Xiong, J. H. Luan, J. M. Pelletier, J. C. Qiao, Q. Wang, L. L. Fan, Y. Ren, Q. S. Zeng, C. T. Liu, C. W. Pao, D. J. Srolovitz, and Y. Yang, A highly distorted ultraelastic chemically complex Elinvar alloy, *Nature (London)* **602**, 251 (2022).
- [14] Z. Rao, P. Tung, R. Xie, Y. Wei, H. Zhang, A. Ferrari, T. P. C. Klaver, F. Körmann, P. T. Sukumar, A. K. da Silva, Y. Chen, Z. Li, D. Ponge, J. Neugebauer, O. Gutfleisch, S. Bauer, and D. Raabe, Machine learning-enabled high-entropy alloy discovery, *Science* **378**, 78 (2022).
- [15] Y. Yao, Q. Dong, A. Brozena, J. Luo, J. Miao, M. Chi, C. Wang, I. G. Kevrekidis, Z. J. Ren, J. Greeley, G. Wang, A. Anapolsky, and L. Hu, High-entropy nanoparticles: Synthesis-structure-property relationships and data-driven discovery, *Science* **376**, eabn3103 (2022).
- [16] Q. Pan, L. Zhang, R. Feng, Q. Lu, K. An, A. C. Chuang, J. D. Poplawsky, P. K. Liaw, and L. Lu, Gradient cell-structured high-entropy alloy with exceptional strength and ductility, *Science* **374**, 984 (2021).
- [17] F. Wang, G. H. Balbus, S. Xu, Y. Su, J. Shin, P. F. Rottmann, K. E. Knippling, J.-C. Stinville, L. H. Mills, O. N. Senkov, I. J. Beyerlein, T. M. Pollock, and D. S. Gianola, Multiplicity of dislocation pathways in a refractory multiprincipal element alloy, *Science* **370**, 95 (2020).
- [18] Z. Lei, X. Liu, Y. Wu, H. Wang, S. Jiang, S. Wang, X. Hui, Y. Wu, B. Gault, P. Kontis, D. Raabe, L. Gu, Q. Zhang, H. Chen, H. Wang, J. Liu, K. An, Q. Zeng, T. G. Nieh, and Z. Lu, Enhanced strength and ductility in a high-entropy alloy via ordered oxygen complexes, *Nature (London)* **563**, 546 (2018).
- [19] S. Shuang, G. J. Lyu, D. Chung, X. Z. Wang, X. Gao, H. H. Mao, W. P. Li, Q. F. He, B. S. Guo, X. Y. Zhong, Y. J. Wang, and Y. Yang, Unusually high corrosion resistance in MoxCrNiCo medium entropy alloy enhanced by acidity in aqueous solution, *J. Mater. Sci. Technol.* **139**, 59 (2023).
- [20] F. X. Zhang, S. Zhao, K. Jin, H. Xue, G. Velisa, H. Bei, R. Huang, J. Y. P. Ko, D. C. Pagan, J. C. Neufeind, W. J. Weber, and Y. Zhang, Local Structure and Short-Range Order in a NiCoCr Solid Solution Alloy, *Phys. Rev. Lett.* **118**, 205501 (2017).
- [21] R. Zhang, S. Zhao, J. Ding, Y. Chong, T. Jia, C. Ophus, M. Asta, R. O. Ritchie, and A. M. Minor, Short-range order and its impact on the crconi medium-entropy alloy, *Nature (London)* **581**, 283 (2020).
- [22] X. Chen, Q. Wang, Z. Cheng, M. Zhu, H. Zhou, P. Jiang, L. Zhou, Q. Xue, F. Yuan, J. Zhu, X. Wu, and E. Ma, Direct observation of chemical short-range order in a medium-entropy alloy, *Nature (London)* **592**, 712 (2021).
- [23] J. Wang, P. Jiang, F. Yuan, and X. Wu, Chemical medium-range order in a medium-entropy alloy, *Nat. Commun.* **13**, 1021 (2022).
- [24] Q.-J. Li, H. Sheng, and E. Ma, Strengthening in multi-principal element alloys with local-chemical-order roughened dislocation pathways, *Nat. Commun.* **10**, 3563 (2019).
- [25] L. Li, Z. Chen, S. Kuroiwa, M. Ito, K. Yuge, K. Kishida, H. Tanimoto, Y. Yu, H. Inui, and E. P. George, Evolution of short-range order and its effects on the plastic deformation behavior of single crystals of the equiatomic Cr-Co-Ni medium-entropy alloy, *Acta Mater.* **243**, 118537 (2022).
- [26] L. Zhou, Q. Wang, J. Wang, X. Chen, P. Jiang, H. Zhou, F. Yuan, X. Wu, Z. Cheng, and E. Ma, Atomic-scale evidence of chemical short-range order in CrCoNi medium-entropy alloy, *Acta Mater.* **224**, 117490 (2022).
- [27] S. Yin, J. Ding, M. Asta, and R. O. Ritchie, Ab initio modeling of the energy landscape for screw dislocations in body-centered cubic high-entropy alloys, *npj Comput. Mater.* **6**, 110 (2020).
- [28] S. Yin, Y. Zuo, A. Abu-Odeh, H. Zheng, X. G. Li, J. Ding, S. P. Ong, M. Asta, and R. O. Ritchie, Atomistic simulations of dislocation mobility in refractory high-entropy alloys and the effect of chemical short-range order, *Nat. Commun.* **12**, 4873 (2021).
- [29] J. Ding, Q. Yu, M. Asta, and R. O. Ritchie, Tunable stacking fault energies by tailoring local chemical order in CrCoNi medium-entropy alloys, *Proc. Natl. Acad. Sci. USA* **115**, 8919 (2018).
- [30] F. Walsh, M. Asta, and R. O. Ritchie, Magnetically driven short-range order can explain anomalous measurements in CrCoNi, *Proc. Natl. Acad. Sci. USA* **118**, e2020540118 (2021).
- [31] B. Xing, X. Wang, W. J. Bowman, and P. Cao, Short-range order localizing diffusion in multi-principal element alloys, *Scr. Mater.* **210**, 114450 (2022).
- [32] Y. Rao and W. A. Curtin, Analytical models of short-range order in FCC and BCC alloys, *Acta Mater.* **226**, 117621 (2022).
- [33] F. Körmann, T. Kostiuchenko, A. Shapeev, and J. Neugebauer, B2 ordering in body-centered-cubic AlNbTiV refractory high-entropy alloys, *Phys. Rev. Mater.* **5**, 053803 (2021).
- [34] S. D. Wang, X. J. Liu, Z. F. Lei, D. Y. Lin, F. G. Bian, C. M. Yang, M. Y. Jiao, Q. Du, H. Wang, Y. Wu, S. H. Jiang, and Z. P. Lu, Chemical short-range ordering and its strengthening effect in refractory high-entropy alloys, *Phys. Rev. B* **103**, 104107 (2021).
- [35] S. Chen, T. Wang, X. Li, Y. Cheng, G. Zhang, and H. Gao, Short-range ordering and its impact on thermodynamic property of high-entropy alloys, *Acta Mater.* **238**, 118201 (2022).
- [36] S. Chen, Z. H. Aitken, S. Pattamatta, Z. Wu, Z. G. Yu, D. J. Srolovitz, P. K. Liaw, and Y. W. Zhang, Simultaneously enhancing the ultimate strength and ductility of high-entropy alloys via short-range ordering, *Nat. Commun.* **12**, 4953 (2021).
- [37] Z. Fan, B. Xing, and P. Cao, Predicting path-dependent diffusion barrier spectra in vast compositional space of multi-principal element alloys via convolutional neural networks, *Acta Mater.* **237**, 118159 (2022).
- [38] X. Wang, F. Maresca, and P. Cao, The hierarchical energy landscape of screw dislocation motion in refractory high-entropy alloys, *Acta Mater.* **234**, 118022 (2022).
- [39] P. Yu, J. P. Du, S. Shinzato, F. S. Meng, and S. Ogata, Theory of history-dependent multi-layer generalized stacking fault energy A modeling of the micro-substructure evolution kinetics in chemically ordered medium-entropy alloys, *Acta Mater.* **224**, 117504 (2022).
- [40] J. P. Du, P. Yu, S. Shinzato, F. S. Meng, Y. Sato, Y. Li, Y. Fan, and S. Ogata, Chemical domain structure and its formation kinetics in CrCoNi medium-entropy alloy, *Acta Mater.* **240**, 118314 (2022).
- [41] B. Yin, S. Yoshida, N. Tsuji, and W. A. Curtin, Yield strength and misfit volumes of NiCoCr and implications for short-range-order, *Nat. Commun.* **11**, 2507 (2020).
- [42] J. Yin, Z. Pei, and M. C. Gao, Neural network-based order parameter for phase transitions and its applications in high-entropy alloys, *Nat. Comput. Sci.* **1**, 686 (2021).

- [43] X. Liu, J. Zhang, and Z. Pei, Machine learning for high-entropy alloys: Progress, challenges and opportunities, *Prog. Mater. Sci.* **131**, 101018 (2023).
- [44] F. Walsh, M. Zhang, R. O. Ritchie, A. M. Minor, and M. Asta, Extra electron reflections in concentrated alloys may originate from planar defects, not short-range order (2022), [arXiv:2210.01277](https://arxiv.org/abs/2210.01277).
- [45] R. Paula Leite and M. de Koning, Nonequilibrium free-energy calculations of fluids using LAMMPS, *Comput. Mater. Sci.* **159**, 316 (2019).
- [46] R. Jinnouchi, F. Karsai, and G. Kresse, Making free-energy calculations routine: Combining first principles with machine learning, *Phys. Rev. B* **101**, 060201(R) (2020).
- [47] T. D. Swinburne, J. Janssen, M. Todorova, G. Simpson, P. Plechac, M. Luskin, and J. Neugebauer, Anharmonic free energy of lattice vibrations in fcc crystals from a mean-field bond, *Phys. Rev. B* **102**, 100101(R) (2020).
- [48] R. Freitas, M. Asta, and M. de Koning, Nonequilibrium free-energy calculation of solids using LAMMPS, *Comput. Mater. Sci.* **112**, 333 (2016).
- [49] R. Freitas, R. E. Rudd, M. Asta, and T. Frolov, Free energy of grain boundary phases: Atomistic calculations for 5(310)[001] grain boundary in Cu, *Phys. Rev. Mater.* **2**, 093603 (2018).
- [50] B. Grabowski, Y. Ikeda, P. Srinivasan, F. Körmann, C. Freysoldt, A. I. Duff, A. Shapeev, and J. Neugebauer, Ab initio vibrational free energies including anharmonicity for multicomponent alloys, *npj Comput. Mater.* **5**, 80 (2019).
- [51] J. G. Kirkwood, Statistical mechanics of fluid mixtures, *J. Chem. Phys.* **3**, 300 (1935).
- [52] Y.-Z. Wang and Y.-J. Wang, Disentangling diffusion heterogeneity in high-entropy alloys, *Acta Mater.* **224**, 117527 (2022).
- [53] D. Frenkel and A. J. C. Ladd, New Monte Carlo method to compute the free energy of arbitrary solids. Application to the fcc and hcp phases of hard spheres, *J. Chem. Phys.* **81**, 3188 (1984).
- [54] F.-H. Cao, Y.-J. Wang, and L.-H. Dai, Novel atomic-scale mechanism of incipient plasticity in a chemically complex CrCoNi medium-entropy alloy associated with inhomogeneity in local chemical environment, *Acta Mater.* **194**, 283 (2020).
- [55] S.-C. Dai, Z.-C. Xie, and Y.-J. Wang, Atomistic interpretation of extra temperature and strain-rate sensitivity of heterogeneous dislocation nucleation in a multi-principal-element alloy, *Int. J. Plast.* **149**, 103155 (2022).
- [56] S. Plimpton, Fast parallel algorithms for short-range molecular dynamics, *J. Comput. Phys.* **117**, 1 (1995).
- [57] A. Stukowski, Visualization and analysis of atomistic simulation data with OVITO—the Open Visualization Tool, *Model. Simul. Mater. Sci. Eng.* **18**, 015012 (2010).
- [58] M. Widom, W. P. Huhn, S. Maiti, and W. Steurer, Hybrid Monte Carlo/Molecular Dynamics Simulation of a Refractory Metal High Entropy Alloy, *Metall. Mater. Trans. A* **45**, 196 (2014).
- [59] R. Alvarez-Donado and A. Antonelli, Splitting up entropy into vibrational and configurational contributions in bulk metallic glasses: A thermodynamic approach, *Phys. Rev. Res.* **2**, 013202 (2020).
- [60] Z.-H. Peng, Z.-Y. Yang, and Y.-J. Wang, Machine learning atomic-scale stiffness in metallic glass, *Extrem. Mech. Lett.* **48**, 101446 (2021).
- [61] F. A. Lindemann, Ueber die berechnung molekularer eigenfrequenzen, *Phys. Z* **11**, 609 (1910).
- [62] K. Sokolowski-Tinten, C. Blome, J. Blums, A. Cavalleri, C. Dietrich, A. Tarasevitch, I. Uschmann, E. Förster, M. Kammler, M. Horn-von Hoegen, and D. von der Linde, Femtosecond X-ray measurement of coherent lattice vibrations near the Lindemann stability limit, *Nature (London)* **422**, 287 (2003).
- [63] F. H. Stillinger, A Topographic View of Supercooled Liquids and Glass Formation, *Science* **267**, 1935 (1995).
- [64] W. K. Kwok, S. Fleshler, U. Welp, V. M. Vinokur, J. Downey, G. W. Crabtree, and M. M. Miller, Vortex Lattice melting in untwinned and twinned single crystals of YBa₂Cu₃O_{7-x}, *Phys. Rev. Lett.* **69**, 3370 (1992).
- [65] Z. H. Jin, P. Gumbsch, K. Lu, and E. Ma, Melting Mechanisms at the Limit of Superheating, *Phys. Rev. Lett.* **87**, 055703 (2001).
- [66] X. Fan, D. Pan, and M. Li, Rethinking Lindemann criterion: A molecular dynamics simulation of surface mediated melting, *Acta Mater.* **193**, 280 (2020).
- [67] G. Zhang, X. Fan, Q. Zhang, Q. Li, Y. Wu, and M. Li, Partial disordering and homogeneous melting in multicomponent systems, *Acta Mater.* **239**, 118281 (2022).